Inorganic Chemistry

pubs.acs.org/IC

Article

Syntheses, Crystal Structures, and Electronic Structures of Quaternary Group IV-Selenide Semiconductors

Subhendu Jana, Eric Gabilondo, Scott McGuigan, and Paul A. Maggard*

Cite This: *Inorg. Chem.* 2024, 63, 6474−6482

Read Online

ACCESS | Metrics & More | Article Recommendations | Supporting Information

ABSTRACT: Early transition-metal chalcogenides have garnered recent attention for their optoelectronic properties for solar energy conversion. Herein, the first Zr-/Hf-chalcogenides with a main group cation, $Ba_9Hf_3Sn_2Se_{19}$ (**1**) and $Ba_8Zr_2SnSe_{13}(Se_2)$ (**2**), have been synthesized. The structure of **1** is formed from isolated $SnSe_4^{4-}$ tetrahedra and distorted $HfSe_6$ octahedra. The latter condense via face-sharing trimeric motifs that are further vertex-bridged into chains of $^{\infty}_{1}[Hf(1)_2Hf(2)Se_{11}]^{10-}$. The structure of **2** is comprised of $SnSe_4^{4-}$ tetrahedra, Se_2^{2-} dimers, and face-sharing dimers of distorted $ZrSe_6$ octahedra. These represent the first reported examples of Hf-/Zr-chalcogenides exhibiting face-sharing octahedra with relatively short Hf−Hf and Zr−Zr distances. Their preparation in high purity is inhibited by their low thermodynamic stability, with calculations showing small calculated ΔU_{dec} values of +7 and +9 meV atom^{-1} for **1** and **2**, respectively. Diffuse reflectance measurements confirm the semiconducting nature of **1** with an indirect band gap of ∼1.4(1) eV. Electronic structure calculations show that the band gap absorptions arise from transitions between predominantly Se-4p valence bands and mixed Hf-5d/Sn-5p or Zr-4d/Sn-5p conduction bands. Optical absorption coefficients were calculated to be more than $\sim 10^5$ cm^{-1} at greater than 1.8 eV. Thus, promising optical properties are demonstrated for solar energy conversion within these synthetically challenging chemical systems.

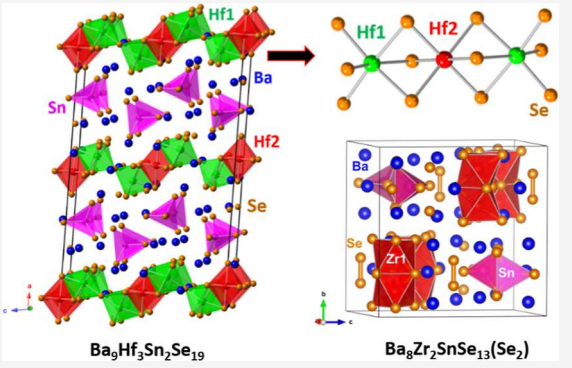

Downloaded via NORTH CAROLINA STATE UNIV on June 11, 2024 at 18:27:32 (UTC).
See https://pubs.acs.org/sharingguidelines for options on how to legitimately share published articles.

1. INTRODUCTION

Exploration of metal chalcogenides with new compositions and structure types continues to be intriguing for solid-state scientists because of their diverse structural chemistry and physical properties. These chemical systems have interesting properties such as thermoelectric properties (e.g., SnSe and $AgCrSe_2$),[1,2] nonlinear optical properties (e.g., $Ba_2AsSbSe_5$ and $KCd_4Ga_5Te_{12}$),[3,4] magnetic properties (e.g., $(BaF_2)_2Fe_{2-x}Q_3$ and $BaLnSn_2Q_6$ (Q = Chalcogenide; Ln = La, Ce, and Pr)),[5,6] superconductivity (e.g., Ta_2Se and FeSe),[7,8] and magneto-resistance (e.g., $CdCr_2Se_4$ and Ag_2Se),[9,10] to name but a few. The rich chemistries for synthetic exploration have been facilitated by the wide and systematic modulation of the structures and compositions possible in metal chalcogenides. Chalcogenides with new structure types can be stabilized because of the (a) diverse catenation possibilities of the chalcogen atoms (*Q*) and (b) the various condensation patterns of *M*-centered polyhedral units, MQ_n (M = metal and n = 3, 4, 5, or 6). For the latter, MQ_n polyhedral units can link together to form extended corner-, edge-, or face-sharing structural motifs. The sharing of polyhedral edges, and especially faces, decreases the stability of a structure owing to the mutual repulsion of the metal cations that are brought into close separation. Understanding the factors leading to new connectivity of the MQ_n polyhedral units, as well as the concomitant impact on the catenation of the chalcogenide anion, is a key to attaining unprecedented structures and for investigating their interplay and impact on physical properties.

Metal-chalcogenide systems based on group-IV cations (i.e., Ti, Zr, and Hf) have been much less explored because of relatively severe synthetic challenges. This is the result of the refractory nature of the binary reactants and the limited thermodynamic stability of the targeted products. For example, the syntheses of Zr- and Hf-containing chalcogenides with the perovskite structure type and composition have been intensely pursued for their optoelectronic properties for solar energy conversion. However, relatively few are yet known, including $SrHfQ_3$ (Q = S or Se) and $BaHfS_3$ in distorted perovskite-type structures.[11−13] As recently reviewed,[14−16] the predicted range of properties in these metal-chalcogenide systems has been identified as highly promising because of their small band gaps extending into the visible-light energy range of ∼1.5 to 2.0 eV, small effective masses of 0.3 to 0.5 m_e*, as well as large optical absorption coefficients of greater than 10^5 cm^{-1}.[14−16] Limiting

Received: January 26, 2024
Revised: March 8, 2024
Accepted: March 12, 2024
Published: March 27, 2024

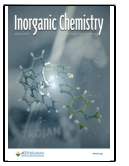

© 2024 American Chemical Society

https://doi.org/10.1021/acs.inorgchem.4c00363
Inorg. Chem. 2024, 63, 6474−6482

current progress has been the observation that the targeted metal chalcogenides in these systems typically exhibit low or no thermodynamic stability. Further, their preparation in high purity shows a sensitive dependence with the reaction conditions.[17] Their synthetic preparation has predominantly involved the reaction of elemental or binary-chalcogenide reactants heated to 1200 °C inside sealed, evacuated quartz ampules. Recent studies have also demonstrated that lower-temperature reactions involving the use of sulfurization agents, e.g., boron sulfides or elemental sulfur, can also be effective in reactions with ternary oxides or other precursors.[18,19]

Beyond the perovskite-type chalcogenides, recent investigations have shown that group-IV chalcogenides forming in alternative structures can possess similar favorable optoelectronic properties. In metal selenides where the perovskite-type structure has yet to be obtained, synthetic attempts have instead yielded the $Ba_8M_2Se_{11}(Se_2)$ (M = Zr, Hf) and $Ba_9Hf_3Se_{14}(Se_2)$ structures.[20,21] These have also shown promising properties for solar energy applications, including optical band gaps of less than ∼2.2 eV, strong optical absorption coefficients, and small carrier effective masses. Motivated initially by subsequent synthetic attempts to prepare a mixed B-site solid-solution "$Ba(M_{0.5}Sn_{0.5})Se_3$" analogue, reactions instead resulted in the discovery of two new quaternary metal chalcogenides that have been characterized by single-crystal X-ray diffraction. Interestingly, both $Ba_9Hf_3Sn_2Se_{19}$ (**1**) and $Ba_8Zr_2SnSe_{13}(Se_2)$ (**2**) described herein represent among the first reported examples of the surprising face-sharing condensation of octahedral units and relatively short M−M distances. Their optical properties, chemical bonding, and thermodynamic stabilities were also investigated with the use of density functional theory (DFT) calculations.

2. EXPERIMENTAL SECTION

2.1. Materials Used and Synthetic Procedures. The following materials were used for the syntheses: Ba rod (99+% purity, Alfa Aesar), Hf powder (99.99% purity, Alfa Aesar), Zr lump (99.99% purity, Alfa Aesar), Sn powder (99.99% purity, Alfa Aesar), and Se lump (99.999% purity, Alfa Aesar). As Ba and Hf are air sensitive, all the chemicals were handled inside an Ar-filled glovebox. The white BaO layer was cleaned before small black chunks of Ba were cut from the Ba rod. It is necessary to slowly heat the reaction mixture to 673 K and hold it at this temperature for 12 to 24 h to prevent the reaction tubes from exploding because of rapid Se volatilization.

2.1.1. Synthesis of $Ba_9Hf_3Sn_2Se_{19}$ Single Crystals. Synthetic attempts to prepare a new chalcogenide perovskite with the formula $BaHf_{0.5}Sn_{0.5}Se_3$ instead produced the new $Ba_9Hf_3Sn_2Se_{19}$. The initial reaction that produced black block-shaped crystals of $Ba_9Hf_3Sn_2Se_{19}$ contained elemental starting materials Ba (78.8 mg, 0.574 mmol), Hf (51.2 mg, 0.287 mmol), Sn (34.1 mg, 0.287 mmol), and Se (135.9 mg, 1.721 mmol) with a 300 mg target product of $BaHf_{0.5}Sn_{0.5}Se_3$. The elements were loaded into a carbon-coated fused silica tube of 12 mm outer diameter (OD) with a 2 mm thickness. The tube was then flame-sealed under $\sim 10^{-4}$ Torr pressure, heated over 8 h to 673 K, and annealed for 12 h in a programmable muffle furnace. The temperature was then ramped to 1173 K in 10 h and soaked for 72 h. The furnace was then switched off and allowed to equilibrate to room temperature by radiative cooling. The ampule was cracked open in the air, revealing a homogeneous-looking lump. The lump was then broken into pieces and investigated under an optical microscope. A few black block-shaped crystals were picked and placed on a carbon tape for elemental analysis using energy-dispersive X-ray (EDX) spectroscopy (Instrument: JEOL SEM 6010LA spectrophotometer). EDX data on selected crystals were recorded by using an accelerating voltage of 20 kV, showing the presence of Ba, Hf, Sn, and Se atoms with an elemental composition of $Ba_9Hf_3Sn_2Se_{19}$ (Ba/Hf/Sn/Se ≈ 9:3:2:19). The crystals were further reproduced from a stoichiometric amount of elemental starting materials of Ba, Hf, Sn, and Se with a target product amount of 600 mg. The composition of the crystals was verified by EDX analysis and unit cell determination by single-crystal X-ray diffraction.

2.1.2. Synthesis of Polycrystalline $Ba_9Hf_3Sn_2Se_{19}$. A high-purity polycrystalline phase of $Ba_9Hf_3Sn_2Se_{19}$ was produced from a synthesis at 1073 K using a two-step solid-state method. In the first step, stoichiometric amounts of Ba (211.3 mg, 1.539 mmol), Hf (91.6 mg, 0.513 mmol), Sn (40.6 mg, 0.342 mmol), and Se (256.5 mg, 3.248 mmol) were loaded into a fused silica tube of 12 mm OD inside the Ar-filled dry glovebox. The tube was then flame-sealed under $\sim 10^{-4}$ Torr pressure and placed inside a programmable muffle furnace. Initially, the furnace temperature was raised to 823 K in 8 h and soaked for 12 h before increasing the temperature over 10 h to 1073 K. The reaction mixture was held at this temperature for 72 h before the furnace was switched off, with radiative cooling of the furnace. The tube was cracked open, and the obtained product was ground inside the Ar-filled glovebox using an Agate mortar pestle and pelletized in the air using a hydraulic press. In the second step, the pellet was loaded inside a 12 mm OD fused silica tube and vacuum sealed under ca. 10^{-4} Torr pressure. The tube was heated at 873 K for 60 h, and the product was then ground inside the glovebox. A small portion of the product was used to analyze the phase purity of the polycrystalline $Ba_9Hf_3Sn_2Se_{19}$ using powder X-ray diffraction (PXRD) data. Other synthetic attempts at lower temperatures instead produced simpler binary and ternary chalcogenides as well as unknown phases.

2.1.3. Synthesis of $Ba_8Zr_2SnSe_{13}(Se_2)$ Single Crystals. Synthetic trials to prepare the Zr-analogue of $Ba_9Hf_3Sn_2Se_{19}$ instead resulted in the formation of crystals of $Ba_8Zr_2SnSe_{13}(Se_2)$. Stoichiometric amounts of Ba (76.1 mg, 0.554 mmol), Zr (16.9 mg, 0.185 mmol), Sn (14.6 mg, 0.0123 mmol), and Se (92.4 mg, 1.170 mmol) were loaded into a 6 mm OD fused silica tube inside an Ar-filled glovebox. The tube was then vacuum sealed by using a flame torch and heated in a muffle furnace by using the same heating profile that was used for the synthesis of $Ba_9Hf_3Sn_2Se_{19}$ crystals. The reaction produced an ingot, which was smashed into small pieces and analyzed under the optical microscope. A few dark-red color crystals were put on carbon tape and the elemental compositions were analyzed using EDX spectroscopy. The EDX analysis showed the presence of Ba, Zr, Sn, and Se with the approximate ratio of 8:2:1:15. After the structure and elemental composition of the $Ba_8Zr_2SnSe_{13}(Se_2)$ crystals were established using single-crystal X-ray diffraction (SCXRD) data, the $Ba_8Zr_2SnSe_{13}(Se_2)$ crystals were reproduced from a stoichiometric amount of elemental starting materials using the same reaction conditions. The yield of $Ba_8Zr_2SnSe_{13}(Se_2)$ crystals was typically only ∼5%. Further synthetic attempts using various heating conditions were unsuccessful in achieving a higher purity of $Ba_8Zr_2SnSe_{13}(Se_2)$. For example, a quenching reaction from 1173 K produced a mixture of unidentified metal chalcogenides.

2.2. Characterization by X-ray Diffraction Techniques. Room temperature data sets from suitable single crystals of $Ba_9Hf_3Sn_2Se_{19}$ and $Ba_8Zr_2SnSe_{13}(Se_2)$ were recorded to establish their crystal structures using a Bruker D8 Venture diffractometer. A graphite monochromatized Mo Kα (λ = 0.71073 Å) radiation source was used to collect the intensity data using a Photon III mixed mode detector. An EDX-analyzed suitable black block-shaped single crystal was picked on a transparent loop under viscous Paratone-N oil, and the crystal was mounted separately on a goniometer head to collect the data. Initially, fast-scan data of 180 frames were collected to judge the crystal quality, and the unit cells were determined for both crystals to collect the whole data set using the APEX3 software.[22] A working current and working voltage of 1.4 mA and 50 kV, respectively, were implemented to collect the intensity data. The intensity data were recorded using a frame width, crystal-to-detector distance, and exposure time of 0.5°, 5 cm, and 4 s/frame, respectively. The collected data were integrated, and the lattice parameters were refined

https://doi.org/10.1021/acs.inorgchem.4c00363
Inorg. Chem. 2024, 63, 6474−6482

using APEX3 software. The multiscan method of the SADABS software was used to perform the absorption correction.[23]

The XPREP program[24] indicated a *C*-centered monoclinic unit cell for the crystal structure of $Ba_9Hf_3Sn_2Se_{19}$. The XPREP program suggested two space groups: *Cc* (noncentrosymmetric) and *C*2/*c* (centrosymmetric). The mean statistics of intensity ($|E^2 - 1|$) value of 1.08 indicated a centrosymmetric space group. So, the crystal structure was solved in the *C*2/*c* space group using direct methods in the SHELX-14 program.[25] The initial solution gave eighteen crystallographically independent atomic sites. The atomic positions were then assigned to respective atoms based on coordination environments, peak heights, and bond distances. The anisotropic displacement parameters, atomic positions, extinction corrections, scale factors, and weight corrections were then refined using the SHELXL program,[26] which used full-matrix least-squares on the F^2 method. The final solution model of the $Ba_9Hf_3Sn_2Se_{19}$ crystal structure gave five Ba, two Hf, one Sn, and ten Se sites. Conversely, for $Ba_8Zr_2SnSe_{13}(Se_2)$, a primitive orthorhombic unit cell was suggested by the XPREP program. The $|E^2 - 1|$ value of 0.952 indicated the centrosymmetric nature of the space group, and the structure was solved by direct methods in the *Pnma* space group based on the reflection conditions. The initial solution gave 17 crystallographically independent atomic sites which could be assigned based on peak heights, bond distances, and coordination environments. The structure was refined similarly as described for $Ba_9Hf_3Sn_2Se_{19}$. The final refined structure solution of $Ba_8Zr_2SnSe_{13}(Se_2)$ showed the presence of five Ba, one Zr, one Sn, and ten Se sites.

The PLATON software package[27] was used to confirm the space group symmetries of both structures. The STRUCTURE TIDY program[28] was used to standardize the atomic positions of both crystal structures. The crystal structure refinement details, bond lengths, and bond angles are provided in Tables 1–3 and Supporting Information.

Table 1. Crystallographic Structural Data and Refinement Details for the $Ba_9Hf_3Sn_2Se_{19}$ (1) and $Ba_8Zr_2SnSe_{13}(Se_2)$ Crystal Structures[a]

	$Ba_9Hf_3Sn_2Se_{19}$	$Ba_8Zr_2SnSe_{13}(Se_2)$
space group	C_{2h}^6–*C*2/*c*	D_{2h}^8–*Pnma*
a (Å)	29.521(5)	12.5617(8)
b (Å)	7.0735(8)	15.9379(9)
c (Å)	19.658(3)	16.2076(8)
β (°)	99.066(6)	
V (Å^3)	4053.6(10)	3244.9 (3)
Z	4	4
ρ (g cm^{-3})	5.750	5.290
μ (mm^{-1})	34.49	27.72
$R(F)$[b]	0.029	0.030
$R_w(F_o^2)$[c]	0.059	0.068
S	1.05	1.05
no. of measured reflections	40,185	45,716
no. of independent reflections	4813	4171
reflections with $I > 2\sigma(I)$	4098	3374

[a] λ = 0.71073 Å, *T* = 300(2) K. [b] $R(F) = \Sigma||F_o| - |F_c||/\Sigma|F_o|$ for $F_o^2 > 2\sigma(F_o^2)$. [c] $R_w(F_o^2) = \{\Sigma[w(F_o^2 - F_c^2)^2]/\Sigma wF_o^4\}^{1/2}$. For $F_o^2 < 0$, $w = 1/[\sigma^2(F_o^2) + (mP)^2 + nP]$, where $P = (F_o^2 + 2F_c^2)/3$. *m* and *n* are 0.0118 and 80.1176 for (1) and 0.025 and 0 for (2), respectively.

A powder XRD data set of the polycrystalline $Ba_9Hf_3Sn_2Se_{19}$ sample was collected at room temperature (300(2) K) using a Cu Kα radiation source of a PANalytical Empyrean X-ray diffractometer. A working voltage of 45 kV and an operating current of 40 mA were used to record the data for the 2θ range of 10 to 75° using a step size of 0.026°.

2.3. Characterization by UV–Vis–NIR Diffuse Reflectance Spectroscopy. The optical absorption data of a ground, homogeneous, polycrystalline sample of $Ba_9Hf_3Sn_2Se_{19}$ were recorded in diffused reflectance mode on a Shimadzu 3600 UV–vis–NIR spectrophotometer over a wavelength range of 1000 nm (1.24 eV) to 250 nm (4.96 eV) using dried $BaSO_4$ as a standard reference. The reflectance data were converted to absorption data using the Kubelka–Munk equation: $\alpha/S = (1 - R)^2/2R$.[29] Here, the terms α, *R*, and *S* are the absorption coefficient, reflectance, and scattering coefficients, respectively. Finally, Tauc plots were used to evaluate the indirect and direct optical transitions of polycrystalline $Ba_9Hf_3Sn_2Se_{19}$[30]

$$(\alpha h\gamma)^n = A(h\gamma - E_g) \quad (1)$$

where the variables *A*, *h*, γ, and E_g represent the respective proportionality constant, Planck's constant, frequency of light, and band gap. The nature of the band gap transition, i.e., whether direct or indirect, is indicated by the value of constant *n*. Values of *n* = 2 and 1/2 are representative of the direct band gap transition and indirect band gap transition, respectively.

2.4. Electronic Structure Calculations. The Vienna ab initio simulation package (VASP) was used to perform DFT calculations using the projector-augmented wave method.[31,32] The exchange–correlation functionals were treated within the r2SCAN meta-generalized gradient approximation.[33] The total energies were converged to 10^{-8} eV/cell with an energy cutoff set to 520 eV in accordance with the PAW pseudopotentials for Ba, Hf, Sn, and Se. Symmetry-constrained geometry relaxations were performed, followed by densities-of-states (DOS) calculations using a Γ-centered 1 × 4 × 2 *k*-point mesh for **1**, and a 5 × 4 × 4 *k*-point mesh for **2**. Band structure calculations were performed next in the standard *k*-point path for their respective crystal systems,[34] with 10 *k*-points calculated along each special Brillouin zone direction. For **1**, the standard path included 90 total *k*-points in the Brillouin zone (along Γ–C|C2–Y2–Γ–M2–D|D2–A–Γ|L2–Γ–V2), while for **2** this comprised a total of 120 *k*-points (along Γ–X–S–Y–Γ–Z–U–R–T–Z|X–U|Y–T|S–R). Individual atomic orbital contributions were projected within both the DOS and band structure plots. The LOBSTER (Local Orbital Suite Toward Electronic Structure Reconstruction) software package,[35–39] version 4.1.0, was used to calculate crystal orbital Hamilton populations (COHPs) for the Hf–Hf, Zr–Zr, Hf–Se, Zr–Se, and Sn–Se interactions in the respective structures out to 4.0 Å.

Table 2. Selected Nearest-Neighbor Interatomic Distances in the $Ba_9Hf_3Sn_2Se_{19}$ Structure

atom pair	bond distance (Å)	atom pair	bond distance (Å)
Hf(1)–Se(7)	2.5277(9)	Hf(2)–Se(1)	2.6357(7) × 2
Hf(1)–Se(2)	2.5299(9)	Hf(2)–Se(9)	2.6395(7) × 2
Hf(1)–Se(10)	2.5748(5)	Hf(2)–Se(8)	2.6497(8) × 2
Hf(1)–Se(8)	2.6968(9)	Sn(1)–Se(3)	2.503(1)
Hf(1)–Se(1)	2.8084(8)	Sn(1)–Se(4)	2.519(1)
Hf(1)–Se(9)	2.8127(8)	Sn(1)–Se(5)	2.521(1)
Hf(1)···Hf(2)	3.3423(5)	Sn(1)–Se(6)	2.541(1)

Table 3. Selected Nearest-Neighbor Interatomic Distances in the $Ba_8Zr_2SnSe_{13}(Se_2)$ Structure

atom pair	bond distance (Å)	atom pair	bond distance (Å)
Zr(1)–Se(2)	2.621(1)	Zr(1)···Zr(1)	3.488(1)
Zr(1)–Se(4)	2.6618(9)	Sn(1)–Se(8)	2.4752(8) × 2
Zr(1)–Se(5)	2.6733(9)	Sn(1)–Se(10)	2.498(1)
Zr(1)–Se(7)	2.6835(9)	Sn(1)–Se(8)	2.4752(8)
Zr(1)–Se(6)	2.706(1)	Se(3)–Se(3)	2.386(2)
Zr(1)–Se(9)	2.758(1)		

3. RESULTS AND DISCUSSION

3.1. Syntheses and Crystal Structure of $Ba_9Hf_3Sn_2Se_{19}$. Single crystals of the first reported alkaline-

https://doi.org/10.1021/acs.inorgchem.4c00363
Inorg. Chem. 2024, 63, 6474–6482

earth metal and Hf-containing quaternary chalcogenide, $Ba_9Hf_3Sn_2Se_{19}$ (**1**), were serendipitously formed while exploring the Ba−Hf−Sn−Se system using high-temperature solid-state synthesis at 1173 K. Initially, the crystals of **1** were obtained with a yield of ∼70% from a reaction composition corresponding to "$BaHf_{0.5}Sn_{0.5}Se_3$". Crystals of **1** could then be reproduced from a reaction mixture containing a stoichiometric amount of elemental starting materials. Additional synthetic attempts to replace Ba with Sr or to replace Se with S or Te failed, and resulted in simpler binary and ternary chalcogenides. A high-purity form of $Ba_9Hf_3Sn_2Se_{19}$ could be synthesized at 1073 K by using a two-step solid-state reaction. The phase purity of the polycrystalline sample was confirmed by powder XRD (Figure S1 in the Supporting Information). The polycrystalline $Ba_9Hf_3Sn_2Se_{19}$ sample was air-stable for at least 1 week, as also assessed by bulk powder XRD analysis.

The crystal structure of **1** was established from single-crystal XRD to form a new structure-type in the centrosymmetric *C*2/*c* space group with unit cell dimensions of a = 29.521(5) Å, b = 7.0735(8), c = 19.658(3), and β = 99.066(6)° and four formula units per unit cell. Listed in Table S1, the asymmetric unit of the $Ba_9Hf_3Sn_2Se_{19}$ crystal structure has eighteen crystallographically independent atomic positions: five Ba, two Hf, one Sn, and ten Se atoms. A polyhedral structural view of the unit cell of $Ba_9Hf_3Sn_2Se_{19}$ and its local structural motifs are shown in Figure 1 and 2, with selected interatomic

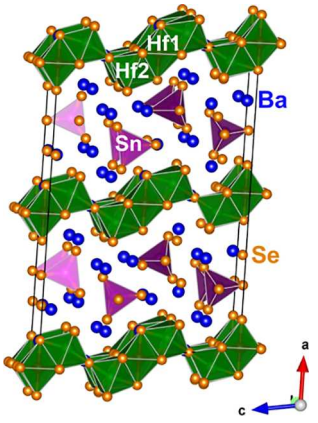

Figure 1. Structural view of the unit cell of $Ba_9Hf_3Sn_2Se_{19}$, with the atom types and the coordinate axis labeled.

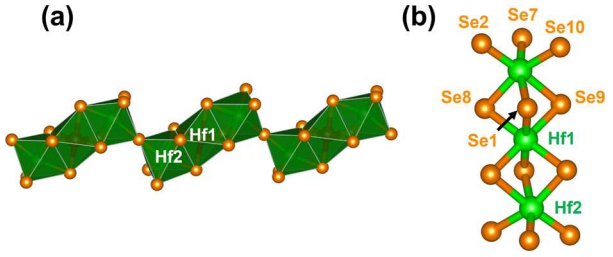

Figure 2. A view of the (a) one-dimensional $^{\infty}_{1}[Hf(1)_2Hf(2)Se_{11}]^{10-}$ chain and (b) the repeating trimeric motif with Hf (green spheres and polyhedra) and Se (orange spheres) atom types labeled.

distances listed in Table 2. As shown in Figures 1 and 2a, its structure is comprised of one-dimensional chains of $^{\infty}_{1}[Hf(1)_2Hf(2)Se_{11}]^{10-}$ extending down the *c*-axis direction. These chains are constructed from a face-sharing trimeric unit, i.e., from one $Hf(1)Se_6$ and two $Hf(2)Se_6$ distorted octahedra. These trimeric units further condense via vertex sharing into chains, as shown in Figure 2a. Within each of the repeating trimeric units, the outer Hf(2) atoms are both distorted from the central Hf(1) atom. These distortions are reflected in the three shorter distances to Se (to Se2, Se7, and Se10 at 2.5299(9), 2.7277(9), and 2.5748(5)Å, respectively) and the three longer distances to Se (to Se1, Se8, and Se9 at 2.8084(8), 2.6968(9), and 2.8127(8)Å, respectively). The central Hf(1) atom exhibits more regular distances to all six Se atoms in the tighter range of 2.6357(9)−2.6497(8)Å. These Hf−Se distances are consistent with comparable distances found in $NaCuHfSe_3$ (2.608(1)−2.788(1) Å),[40] $SrHfSe_3$ (2.559(2)−2.720(9) Å),[11] $NaCuHf_2Se_5$ (2.65(1)−2.701(2) Å),[41] and $Tl_2PbHfSe_4$ (2.6804(5)−2.7296(5) Å).[42] Neighboring chains are packed within layers and separated by $SnSe_4^{4-}$ tetrahedra down the *a*-axis direction with charge balancing achieved by barium cations. The Sn−Se distances fall within the range of 2.5027(10) to 2.5411(10) Å, consistent with previously reported distances in $Ba_7Sn_3Se_{13}$ (2.477(1)−2.534(1) Å),[43] $BaCu_2SnSe_4$ (2.509(3)−2.545(2) Å),[44] and $Sr_4Sn_2Se_9$ (2.503(3)−2.636(3) Å).[45] The details of the Ba coordination environment are provided in the Supporting Information.

To the best of our knowledge, the structure of **1** contains the first reported face-sharing polyhedral motif in a Hf-based chalcogenide. Owing to the mutual repulsion of metal cations, face sharing is generally considered the least energetically favorable condensation pathway of octahedral units. Because of the face sharing between $Hf(1)Se_6$ and $Hf(2)Se_6$ octahedra, the distance of 3.3423(5)Å between Hf(1) and Hf(2) atoms is shorter than typical Hf···Hf distances observed in vertex-shared and edge-shared Hf-containing chalcogenides. The significant intraoctahedral distortions of the Hf(2) atoms likely stem from an energetic gain for an increased Hf−Hf separation across their shared octahedral face. By comparison, the Pauling covalent radius of a Hf atom is ∼1.44 Å.[46] Thus, the Hf(1)···Hf(2) distance in $Ba_{19}Hf_3Sn_2Se_{19}$ is larger than the sum of Pauling covalent radii of two Hf atoms (∼2.88 Å), indicating the absence of significant Hf−Hf bonding. Results of bond valence sum calculations (Table S3 in the Supporting Information) are consistent with closed-shell oxidation states of the ions, i.e., Ba^{2+}, Hf^{4+}, Sn^{4+}, and Se^{2-}, giving the charge-balanced formula of $(Ba^{2+})_9(Hf^{4+})_3(Sn^{4+})_2(Se^{2-})_{19}$. The chemical bonding is further probed using DFT calculations below.

3.2. Syntheses and Crystal Structure of $Ba_8Zr_2SnSe_{13}(Se_2)$. Dark red block-shaped single crystals of $Ba_8Zr_2SnSe_{13}(Se_2)$ (**2**) were serendipitously synthesized during the preparation of the Zr-analogue of $Ba_9Hf_3Sn_2Se_{19}$ at 1173 K. Compound **2** was obtained as the first known example to be reported in the Ba−Zr−Sn−Se system with a slightly different chemical composition and distinct structure type. The crystals of **2** were rationally reproduced from stoichiometric elemental starting materials at 1173 K with a yield of ∼5%, which typically contained a mixture of constituent phases such as Ba_2SnSe_4, $BaZrSe_3$, and BaSe. Given the similarities of morphologies and the dark-reddish color of nearly all the products in the crystalline mixture, a manual separation of the crystallites of **2** for property measurements was not possible.

Single-crystal data from selected crystals of **2** showed that it crystallizes in the centrosymmetric *Pnma* space group with unit cell dimensions of a = 12.5617(8) Å, b = 15.9379(9) Å, c = 16.2076(8) Å, and Z = 4, with crystallographically independent atomic positions as listed in Table S2 and selected interatomic

https://doi.org/10.1021/acs.inorgchem.4c00363
Inorg. Chem. 2024, 63, 6474−6482

distances in Table 3. The structure of **2** is pseudo zero-dimensional and comprised of $Zr_2Se_9^{10-}$ octahedral dimers and $SnSe_4^{4-}$ tetrahedral units, which are separated by the dimeric Se_2^{2-} units and Ba atoms, as shown in a view of the unit cell in Figures 3 and 4a. The $Zr_2Se_9^{10-}$ octahedral dimers are formed

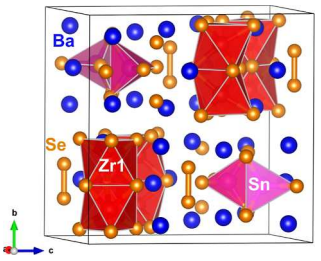

Figure 3. Polyhedral structural views of the unit cell of $Ba_8Zr_2SnSe_{13}(Se_2)$ with the atom types and coordinate axis labeled.

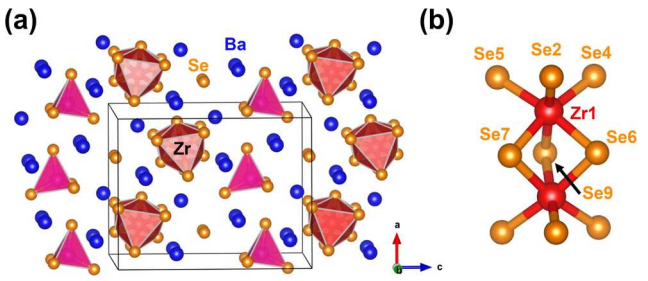

Figure 4. For $Ba_8Zr_2SnSe_{13}(Se_2)$, (a) structural view of the packing of the isolated $SnSe_4^{4-}$ tetrahedra (purple polyhedra) and face-sharing $Zr_2Se_9^{10-}$ octahedral dimers (red spheres and polyhedra) and (b) local coordination environment of the octahedral dimer.

by the face-sharing condensation of two $Zr(1)Se_6$ distorted octahedral units, as illustrated in Figure 4b. As a result, a relatively short Zr···Zr distance occurs across the shared octahedral face at 3.488(1)Å, as found similarly for the Hf···Hf distance in the structure of **1**. In the structure of **2**, the Zr−Se distances of $Zr(1)Se_6$ octahedra range from 2.621(1) to 2.758(1) Å, consistent with previously reported distances in the structures of $Ba_8Zr_2Se_{11}(Se_2)$ (2.6337(7)−2.7940(7) Å)[21] and $Ba_{15}Zr_{14}Se_{42}$ (2.612(4)−2.769(4) Å).[47]

The local coordination geometry of each of the Sn atoms consists of bonds to four Se atoms (two Se(1) atoms, one Se(8) atom, and one Se(10) atom), forming isolated $SnSe_4^{4-}$ tetrahedra. The Sn(1)−Se distances of 2.4752(8)−2.498(1)Å in the $Sn(1)Se_4$ tetrahedral units can be compared with the Sn−Se distances as described above in Section 3.2. By contrast, the structure of **2** contains relatively short Se−Se distances of 2.386(2) Å between two neighboring Se(3) atoms, thus indicating the presence of Se_2^{2-} dimeric units. By comparison, the sum of Pauling covalent radii of two Se atoms is 2.34 Å (1.17 Å + 1.17 Å).[46] This distance for the Se_2^{2-} dimeric units agrees well with prior reported Se−Se distances of 2.4018(7) Å in the structure of $Ba_8Hf_2Se_{11}(Se_2)$[20] and of 2.378(2) Å in $Ba_2Ag_2Se_2(Se_2)$.[48] All bond distances are consistent with additional Se atoms having a −2 oxidation state. The oxidation states of the Ba, Zr, and Sn metal cations as +2, +4, and +4, respectively, yield the charge-balanced formula of $(Ba^{2+})_8(Zr^{4+})_2(Sn^{4+})(Se^{2-})_{13}(Se_2^{2-})$.

3.3. Thermodynamic Calculations of Stability. Recent studies have revealed the synthetic challenges in attaining high-purity forms of metal chalcogenides that contain tetravalent cations such as Zr(IV) and Hf(IV).[17,19] For example, many perovskite-type selenides, such as $SrMSe_3$ (M = Zr, Hf), show limited to no thermodynamic stability.[49] Prior studies have demonstrated that thermodynamic stabilities can be calculated with an accuracy of ∼24 meV atom^{-1} with respect to decomposition reactions to the stable binary and ternary chalcogenides.[50,51] For example, the decomposition of **1** can be estimated by eq 2

$$Ba_9Hf_3Sn_2Se_{19} \rightarrow 2Ba_2SnSe_4 + 3HfSe_2 + 5BaSe \quad (2)$$

Using this approach, the thermodynamic stabilities of **1** and **2**, as well as their hypothetical Zr- and Hf-based analogues (i.e., the $Ba_9Zr_3Sn_2Se_{19}$ and $Ba_8Hf_2SnSe_{13}(Se_2)$ compositions), were assessed using total energy calculations by DFT methods and employing *meta*-GGA (r2scan) functionals.[33] The results are listed in Table 4 below. When compared to the simple binaries

Table 4. Results of Stability Calculations of 1 and 2 (and Their Hypothetical M = Zr and Hf Analogues) vs Decomposition into Stoichiometric Mixtures of Binary and Ternary Selenides

compound	decomposition products (molar ratio)	ΔU_{dec} (meV atom^{-1})	
		M = Hf	M = Zr
$Ba_9M_3Sn_2Se_{19}$ (**1**; M = Hf)	$SnSe_2$, MSe_2, BaSe (2:3:9)	+51.7	+50.5
	Ba_2SnSe_4, MSe_2, BaSe (2:3:5)	+24.9	+23.7
	Ba_2SnSe_4, $BaMSe_3$, BaSe (2:3:2)	+6.8	+2.4
$Ba_8M_2SnSe_{13}(Se_2)$ (**2**; M = Zr)	$Ba_8M_2Se_{11}(Se_2)$, $SnSe_2$ (1:1)	+11.6	+9.0

$SnSe_2$, MSe_2 (M = Zr, Hf), and BaSe, the $Ba_9M_3Sn_2Se_{19}$ compounds are relatively thermodynamically stable by ∼+50−52 meV atom^{-1}. However, when compared to compounds closer on the convex hull of chemical compositions, their stability is significantly reduced and/or borderline. For example, the inclusion of possible decomposition products containing Ba_2SnSe_4 reduces this stability by 50% to only +24−25 meV atom^{-1}. Decomposition products also including the $BaMSe_3$ ternaries further reduce the calculated stability to close to zero at +2 and +7 meV atom^{-1} for M = Zr and Hf, respectively. These results agree with experimental product distributions, with **1** being very difficult to isolate in high purity and the hypothetical M = Zr not so far being synthesized using similar reaction conditions.

Conversely, for **2** and its hypothetical M = Hf analogue, the closest chemical composition on the convex hull that determines the decomposition pathway are the previously reported $Ba_8M_2Se_{11}(Se_2)$ compounds that also contain dimeric $(Se_2)^{2-}$ units in their structures.[20] This is also consistent with the observed product distributions in the typical reactions for **2**. For example, the decomposition of **2** can be estimated by eq 3

$$Ba_8Zr_2SnSe_{13}(Se_2) \rightarrow Ba_8Zr_2Se_{11}(Se_2) + SnSe_2 \quad (3)$$

The calculated decomposition energies of $Ba_8M_2SnSe_{13}(Se_2)$ are +9.0 and +11.6 meV atom^{-1}, respectively, for M = Zr and Hf. Their low stability reveals the origin of the synthetic difficulties in attaining these compounds in high purity. Thus, these results show that successful synthetic trials may prove

https://doi.org/10.1021/acs.inorgchem.4c00363
Inorg. Chem. 2024, 63, 6474−6482

more productive when starting from the elemental reactants and with careful avoidance of the stable ternary chalcogenides.

3.4. Optical Band Gaps and Electronic Structures.

Solid-state UV−vis absorption data were collected for a polycrystalline sample of $Ba_9Hf_3Sn_2Se_{19}$ at room temperature (300 K) over the wavelength region of 250 nm (4.96 eV) to 1000 nm (1.24 eV). As shown in Figure 5, Tauc plots were

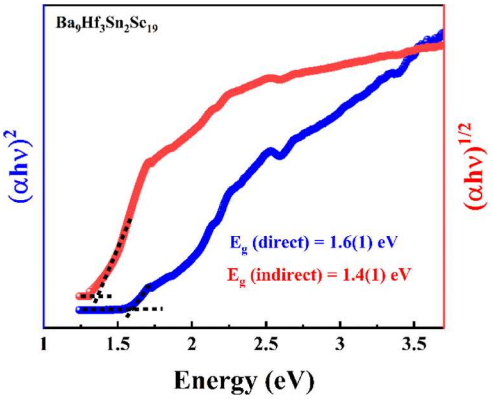

Figure 5. Tauc plot of the UV−vis DRS spectra of polycrystalline $Ba_9Hf_3Sn_2Se_{19}$ with the extrapolated optical absorption edges labeled.

used to attain an estimate of the indirect and direct band gap transitions of polycrystalline $Ba_9Hf_3Sn_2Se_{19}$ (**1**). It was found that the polycrystalline $Ba_9Hf_3Sn_2Se_{19}$ sample has direct and indirect transitions of 1.6(1) and 1.4(1) eV, respectively, which indicates its semiconducting nature. This is also in good agreement with the dark gray color of the polycrystalline sample of $Ba_9Hf_3Sn_2Se_{19}$.

Chalcogenide-based semiconductors have received a surging number of investigations into their promising properties for solar energy conversion, such as their low effective masses, strong band edge absorption ($\alpha > 10^5$), stability in air and water, and band gaps that extend deep into the visible-light wavelengths (~1.2 to 2.4 eV).[14−16] While most prior studies have focused on perovskite-type chalcogenides, it is yet unclear what impact alternative structures have on their potential optoelectronic properties. This is especially important considering the diversity of possible impacts that changes in polyhedral connectivity and chalcogenide catenation in these systems can have on their properties. DFT calculations were used to probe the electronic structures of **1** and **2**, including the elemental contributions to their conduction and valence bands (VBs) and the magnitudes of the optical absorption coefficients.

The structures of both **1** and **2** were geometry optimized, followed by calculations of their DOSs and band structures, separately. Plotted in Figure 6a,c are the DOS for each structure with the atomic orbital contributions outlined for Sn (blue), Ba (yellow), Se (green), and either Hf (red) or Zr (purple). Both are consistent with their semiconducting nature, generally indicating band gaps for each of <2 eV. The VBs are predominantly Se-based in character. Conversely, the conduction band (CB) edges are mainly Zr- or Hf-based states, respectively, which are also mixed to a smaller extent with Sn- and Se-based states at higher energies. The calculated band structures in Figures S6 and S7 indicate that the shortest band gap transitions for both are indirect by about ~0.1 eV, consistent with UV−vis DRS data. The band gap for **1** is found to be ~1.08 eV and underestimated as compared to the

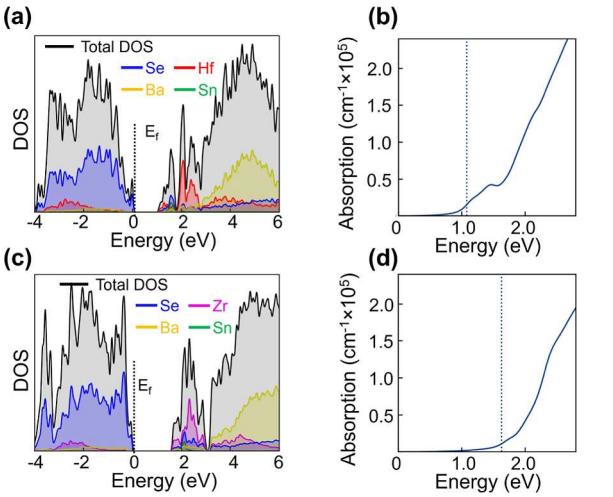

Figure 6. Calculated electronic DOS plots for the (a) $Ba_9Hf_3Sn_2Sn_{19}$ and (c) $Ba_8Zr_2SnSe_{13}(Se_2)$ crystal structures and their respective optical absorption coefficients vs energy (b,d). The Fermi levels are located at 0 K, while in (b,d) the band gap energy is labeled by the dashed blue line.

measured value of ~1.4 eV. The calculated band gap for **2** is ~1.20 eV, which is also underestimated compared with the red color of the $Ba_8Zr_2SnSe_{13}(Se_2)$ crystals. Within the CB of each, the smallest electron effective masses were ~0.8 m_e* ($\Gamma \rightarrow C$) in **1** and a higher ~1.6 m_e* ($\Gamma \rightarrow X$) in **2**. This is consistent with the more disperse CBs in **1**. This also compares similarly to electron effective masses within the intensely investigated perovskite-type compounds for $BaHfS_3$ and $BaZrS_3$ of ~0.94 and ~0.41 m_e*, respectively.[52] The more disperse VBs of **2**, by contrast, also yield a small, calculated hole effective mass of ~0.5 m_h* ($\Gamma \rightarrow X$). This likely results from the electron-deficient nature of the $Ba_8Zr_2SnSe_{13}(Se_2)$ compound and the onset of Se−Se bonding, and thus a greater dispersion of its VB. The optical absorption coefficients, plotted in Figure 6b,d, were calculated to reach >10^5 cm^{-1} for energies above ~2.0 eV for each. The rise in the optical absorption coefficient with increasing energies is steeper for **1**, with a lower-energy edge stemming from its indirect band gap. These values are similar to those reported for chalcogenide perovskites such as $BaZrS_3$, demonstrating that their attractive optoelectronic properties are not restricted to perovskite-type compositions and structures.

To evaluate the chemical bonding of **1** and **2**, COHPs were calculated using DFT methods for their geometry-relaxed structures. This enables an analysis of the impact of the coordination environments and structural connectivities on the interatomic bonding for each of the Hf−Se, Sn−Se, Hf−Hf, and Se−Se bonding interactions in **1** and Zr−Se, Sn−Se, Zr−Zr, and Se−Se in **2**. The results are shown in Figure 7, with the bonding (+) and antibonding (−) regions plotted as a function of the energy. Both structures achieve an optimization of the metal-selenide bonds, i.e., Sn−Se, Hf−Se, and Zr−Se, with electron filling of only bonding states below their Fermi levels. Their corresponding antibonding states dominate at the bottom of the CB. Additional contributions at the bottom of the CBs arise from bonding Hf−Hf interactions in **1** and bonding Zr−Zr interactions in **2**. This reflects the short interatomic distances across the shared octahedral faces in each structure. A small amount of Hf−Hf and Zr−Zr bonding occurs upon mixing with the Se-based states in the VB as a

https://doi.org/10.1021/acs.inorgchem.4c00363
Inorg. Chem. 2024, 63, 6474−6482

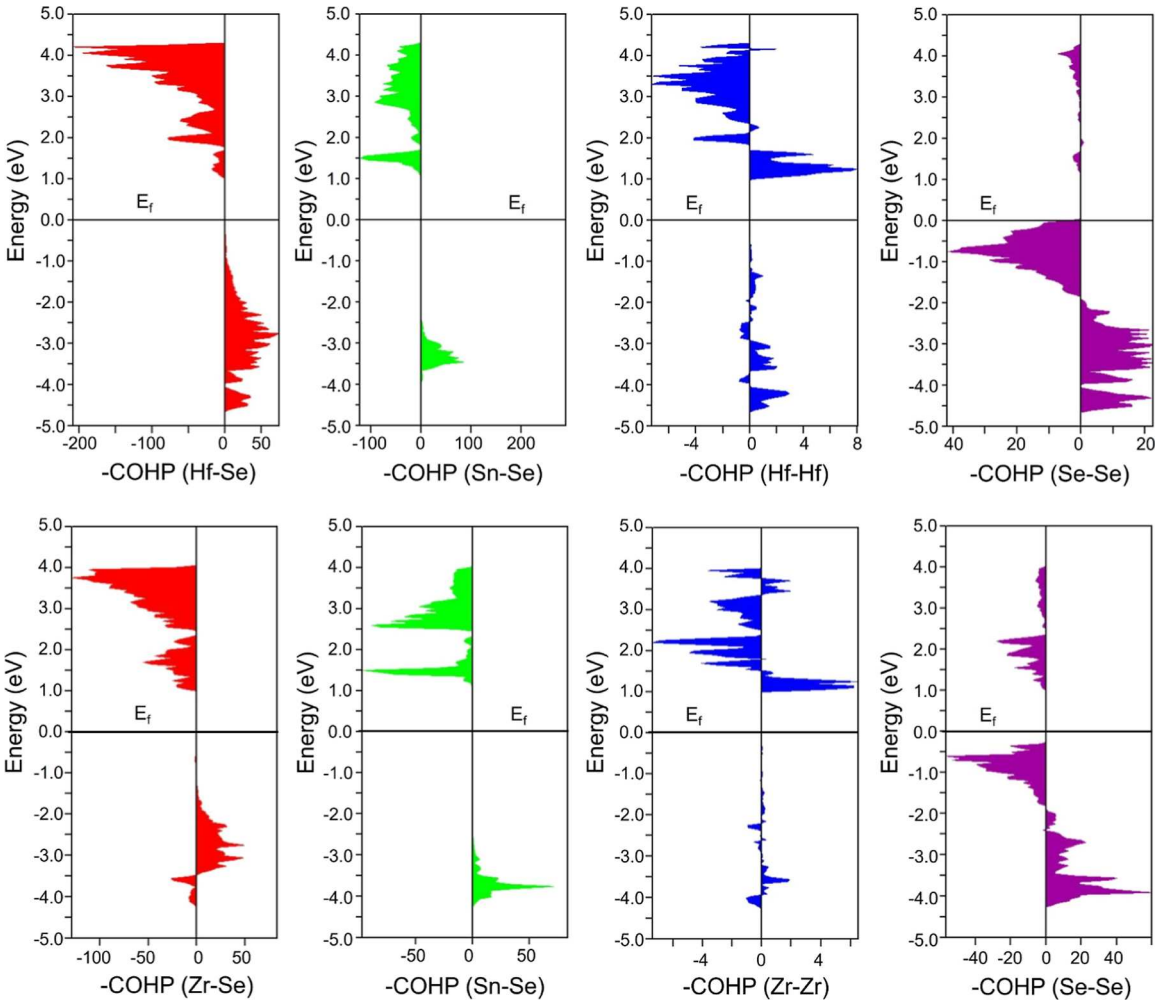

Figure 7. Plots of COHP for the pairwise interactions in (upper) $Ba_9Hf_3Sn_2Se_{19}$ and (lower) $Ba_8Zr_2SnSe_{13}(Se_2)$ with the Fermi levels (E_f) labeled on each.

result of the covalent bonding. Calculation of their crystal orbital bond indices (COBIs), which is the equivalent for bond order in extended systems,[53] yields relatively small values of ∼0.095 for Hf−Hf and ∼0.092 for Zr−Zr interactions. For the Se−Se interactions, a comparison of the COHP curves of **1** and **2** shows only evidence for the formation of Se−Se dimers in the latter. This arises from its more electron-deficient composition leading to empty antibonding interactions not filled at the bottom of the CB and is consistent with the short Se−Se dimer distances in its structure. The COBI of this interaction was calculated to be ∼0.901 and is consistent with the formation of singly bonded Se−Se dimers as anticipated also from bond distances and charge-balancing considerations.

4. CONCLUSIONS

Two new quaternary chalcogenides, $Ba_9Hf_3Sn_2Se_{19}$ (**1**) and $Ba_8Zr_2SnSe_{13}(Se_2)$ (**2**), were synthesized by high-temperature solid-state reactions in evacuated quartz tubes. These represent among the first reported examples of alkaline earth and Hf/Zr-containing chalcogenides. The structures of both were characterized by single-crystal X-ray diffraction and exhibit new structure types, with **1** containing isolated $SnSe_4$ tetrahedra and one-dimensional chains of $^{\infty}_{1}[Hf(1)_2Hf(2)Se_{11}]^{10-}$ and **2** comprised of $SnSe_4$ tetrahedra, dimeric Se_2^{2-} units, as well as dimeric $Zr_2Se_9^{10-}$ motifs. Surprisingly, both contain face-sharing octahedra that lead to relatively short Hf···Hf or Zr···Zr distances. The calculated crystal orbital bond indices for these were relatively small, at ∼0.091 and ∼0.095, respectively, and consistent with the absence of significant metal−metal bonding. Both exhibit borderline stability with respect to decomposition to known binary and ternary chalcogenides, leading to severe synthetic difficulties in their preparation in a high-purity polycrystalline form. Optical diffuse reflectance measurements confirm the semiconducting nature of **1** with a small band gap of ∼1.4(1) eV. Electronic structure calculations reveal that both possess large optical absorption coefficients of more than $\sim 10^5$ cm^{-1} at >1.8 eV and small effective masses of ∼0.4 to 0.8 m_e*. Thus, the results highlight not only the promising optical properties of these quaternary chalcogenides for solar energy conversion but also the concomitant experimental challenges in synthesizing them in high-purity form.

■ ASSOCIATED CONTENT

Supporting Information

The Supporting Information is available free of charge at https://pubs.acs.org/doi/10.1021/acs.inorgchem.4c00363.

Crystallographic data files of $Ba_9Hf_3Sn_2Se_{19}$ and $Ba_8Zr_2SnSe_{13}(Se_2)$ structures are available by request to the Cambridge Crystallographic Data Centre

https://doi.org/10.1021/acs.inorgchem.4c00363
Inorg. Chem. 2024, 63, 6474−6482

(CCDC) in the form of crystallographic information files with CCDC numbers of 2287814 and 2322227, respectively. The data can be accessed from CCDC (https://www.ccdc.cam.ac.uk/) at no charge; SEM data of the elemental composition, the Ba coordination environment, the atomic displacement parameters, and the metric details of each crystal structure (PDF)

AUTHOR INFORMATION

Corresponding Author

Paul A. Maggard − *Department of Chemistry, North Carolina State University, Raleigh, North Carolina 27695, United States;* orcid.org/0000-0002-3909-1590; Email: Paul_Maggard@ncsu.edu

Authors

Subhendu Jana − *Department of Chemistry, North Carolina State University, Raleigh, North Carolina 27695, United States*

Eric Gabilondo − *Department of Chemistry, North Carolina State University, Raleigh, North Carolina 27695, United States*

Scott McGuigan − *Department of Chemistry, North Carolina State University, Raleigh, North Carolina 27695, United States;* orcid.org/0000-0002-9554-0151

Complete contact information is available at: https://pubs.acs.org/10.1021/acs.inorgchem.4c00363

Notes

The authors declare no competing financial interest.

ACKNOWLEDGMENTS

The authors acknowledge primary support for this work from the National Science Foundation (DMR-2317605). This work was performed in part by the Molecular Education, Technology and Research Innovation Center (METRIC) at NC State University, which is supported by the State of North Carolina. This work was also performed in part at the Analytical Instrumentation Facility (AIF) at North Carolina State University, which is supported by the State of North Carolina and the National Science Foundation (award number ECCS-2025064). The AIF is a member of the North Carolina Research Triangle Nanotechnology Network (RTNN), a site in the National Nanotechnology Coordinated Infrastructure (NNCI). The authors acknowledge the computing resources provided by the North Carolina State University High Performance Computing Services Core Facility.

REFERENCES

(1) Zhao, L.-D.; Chang, C.; Tan, G.; Kanatzidis, M. G. SnSe: A Remarkable New Thermoelectric Material. *Energy Environ. Sci.* **2016**, *9*, 3044−3060.

(2) Gascoin, F.; Maignan, A. Order-Disorder Transition in $AgCrSe_2$: A New Route to Efficient Thermoelectrics. *Chem. Mater.* **2011**, *23*, 2510−2513.

(3) Iyer, A. K.; Cho, J. B.; Waters, M. J.; Cho, J. S.; Oxley, B. M.; Rondinelli, J. M.; Jang, J. I.; Kanatzidis, M. G. Ba_2MAsQ_5 (Q = S and Se) Family of Polar Structures with Large Second Harmonic Generation and Phase Matchability. *Chem. Mater.* **2022**, *34*, 5283−5293.

(4) Sun, M.; Xing, W.; Chen, S. K.; Li, C.; Liu, W.; Lee, M.-H.; Yao, J. $ACd_4Ga_5Te_{12}$ (A = K, Rb, Cs): Tellurides with a Strong Nonlinear Optical Response and Purple Emission. *Chem. Mater.* **2023**, *35*, 7218−7228.

(5) Sturza, M.; Allred, J. M.; Malliakas, C. D.; Bugaris, D. E.; Han, F.; Chung, D. Y.; Kanatzidis, M. G. Tuning the Magnetic Properties of New Layered Iron Chalcogenides $(BaF)_2Fe_{2-x}Q_3$ (Q = S, Se) by Changing the Defect Concentration on the Iron Sublattice. *Chem. Mater.* **2015**, *27*, 3280−3290.

(6) Feng, K.; Zhang, X.; Yin, W.; Shi, Y.; Yao, J.; Wu, Y. New Quaternary Rare-Earth Chalcogenides $BaLnSn_2Q_6$ (Ln = Ce, Pr, Nd, Q = S; Ln = Ce, Q = Se): Synthesis, Structure, and Magnetic Properties. *Inorg. Chem.* **2014**, *53*, 2248−2253.

(7) Gui, X.; Górnicka, K.; Chen, Q.; Zhou, H.; Klimczuk, T.; Xie, W. Superconductivity in Metal-Rich Chalcogenide Ta_2Se. *Inorg. Chem.* **2020**, *59* (9), 5798−5802.

(8) Margadonna, S.; Takabayashi, Y.; McDonald, M. T.; Kasperkiewicz, K.; Mizuguchi, Y.; Takano, Y.; Fitch, A. N.; Suard, E.; Prassides, K. Crystal Structure of the New $FeSe_{1-x}$ Superconductor. *Chem. Commun.* **2008**, 5607−5609.

(9) Bongers, P. F.; Haas, C.; van Run, A. M. J. G.; Zanmarchi, G. Magnetoresistance in Chalcogenide Spinels. *J. Appl. Phys.* **1969**, *40*, 958−963.

(10) Xu, R.; Husmann, A.; Rosenbaum, T. F.; Saboungi, M.-L.; Enderby, J. E.; Littlewood, P. B. Large Magnetoresistance in Non-Magnetic Silver Chalcogenides. *Nature* **1997**, *390*, 57−60.

(11) Moroz, N. A.; Bauer, C.; Williams, L.; Olvera, A.; Casamento, J.; Page, A. A.; Bailey, T. P.; Weiland, A.; Stoyko, S. S.; Kioupakis, E.; Uher, C.; Aitken, J. A.; Poudeu, P. F. P. Insights on the Synthesis, Crystal and Electronic Structures, and Optical and Thermoelectric Properties of $Sr_{1-x}Sb_xHfSe_3$ Orthorhombic Perovskite. *Inorg. Chem.* **2018**, *57*, 7402−7411.

(12) Hanzawa, K.; Iimura, S.; Hiramatsu, H.; Hosono, H. Material Design of Green-Light-Emitting Semiconductors: Perovskite-Type Sulfide $SrHfS_3$. *J. Am. Chem. Soc.* **2019**, *141*, 5343−5349.

(13) Lelieveld, R.; IJdo, D. J. W. Sulphides with the $GdFeO_3$ Structure. *Acta Crystallogr., Sect. B: Struct. Crystallogr. Cryst. Chem.* **1980**, *36*, 2223−2226.

(14) Basera, P.; Bhattacharya, S. Chalcogenide Perovskites (ABS_3; A = Ba, Ca, Sr; B = Hf, Sn): An Emerging Class of Semiconductors for Optoelectronics. *J. Phys. Chem. Lett.* **2022**, *13*, 6439−6446.

(15) Raj, R.; Singh, R.; Guin, M. Chalcogenide Perovskite, An Emerging Photovoltaic Material: Current Status and Future Perspectives. *ChemistrySelect* **2023**, *8*, No. e202303550.

(16) Tiwari, D.; Hutter, O. S.; Longo, G. Chalcogenide Perovskites for Photovoltaics: Current Status and Prospects. *J. Phys.: Energy* **2021**, *3*, 034010.

(17) Kayastha, P.; Tiwari, D.; Holland, A.; Hutter, O. S.; Durose, K.; Whalley, L. D.; Longo, G. High-Temperature Equilibrium of 3D and 2D Chalcogenide Perovskites. *Sol. RRL* **2023**, *7*, 2201078.

(18) Bystrický, R.; Tiwari, S. K.; Hutár, P.; Vančo, L.; Sýkora, M. Synthesis of Sulfide Perovskites by Sulfurization with Boron Sulfides. *Inorg. Chem.* **2022**, *61*, 18823−18827.

(19) Turnley, J. W.; Vincent, K. C.; Pradhan, A. A.; Panicker, I.; Swope, R.; Uible, M. C.; Bart, S. C.; Agrawal, R. Solution Deposition for Chalcogenide Perovskites: A Low-Temperature Route to $BaMS_3$ Materials (M = Ti, Zr, Hf). *J. Am. Chem. Soc.* **2022**, *144*, 18234−18239.

(20) Jana, S.; Gabilondo, E. A.; Maggard, P. A. Two New Multinary Chalcogenides with $(Se_2)^{2-}$ Dimers: $Ba_8Hf_2Se_{11}(Se_2)$ and $Ba_9Hf_3Se_{14}(Se_2)$. *J. Solid State Chem.* **2024**, *329*, 124376.

(21) Srivastava, K.; Shahid, O.; Ray, A. K.; Deepa, M.; Niranjan, M. K.; Prakash, J. $Ba_8Zr_2Se_{11}(Se_2)$: The First Polychalcogenide of the Ternary Ba-Zr-Q (Q = S/Se/Te) System. *J. Solid State Chem.* **2023**, *328*, 124344.

(22) *APEX3: Program for Data Collection on Area Detectors*; Bruker AXS, Inc.: Madison, WI, 2009.

(23) Sheldrick, G. M. *SADABS*; Bruker, AXS, Inc.: Madison, Wisconsin, USA, 2008.

(24) Sheldrick, G. M. *XPREP Version 2008/2*; Bruker AXS Inc.: Madison, 2018.

(25) Sheldrick, G. M. Crystal Structure Refinement with SHELXL. *Acta Crystallogr., Sect. C: Struct. Chem.* **2015**, *71*, 3−8.

(26) Sheldrick, G. M. A Short History of SHELX. *Acta Crystallogr., Sect. A: Found. Crystallogr.* **2008**, *64*, 112−122.
(27) Spek, A. L. Single-Crystal Structure Validation with the Program PLATON. *J. Appl. Crystallogr.* **2003**, *36*, 7−13.
(28) Gelato, L. M.; Parthé, E. STRUCTURE TIDY - a Computer Program to Standardize Crystal Structure Data. *J. Appl. Crystallogr.* **1987**, *20*, 139−143.
(29) Kortüm, G. *Reflectance Spectroscopy: Principles, Methods, Applications*; Springer-Verlag: New York, 1969.
(30) Makuła, P.; Pacia, M.; Macyk, W. How To Correctly Determine the Band Gap Energy of Modified Semiconductor Photocatalysts Based on UV-Vis Spectra. *J. Phys. Chem. Lett.* **2018**, *9*, 6814−6817.
(31) Kresse, G.; Furthmüller, J. Efficient Iterative Schemes for Ab Initio Total-Energy Calculations Using a Plane-Wave Basis Set. *Phys. Rev. B: Condens. Matter Mater. Phys.* **1996**, *54*, 11169−11186.
(32) Kresse, G.; Furthmüller, J. Efficiency of Ab-Initio Total Energy Calculations for Metals and Semiconductors Using a Plane-Wave Basis Set. *Comput. Mater. Sci.* **1996**, *6*, 15−50.
(33) Furness, J. W.; Kaplan, A. D.; Ning, J.; Perdew, J. P.; Sun, J. Accurate and Numerically Efficient r^2SCAN Meta-Generalized Gradient Approximation. *J. Phys. Chem. Lett.* **2020**, *11*, 8208−8215.
(34) Hinuma, Y.; Pizzi, G.; Kumagai, Y.; Oba, F.; Tanaka, I. Band Structure Diagram Paths Based on Crystallography. *Comput. Mater. Sci.* **2017**, *128*, 140−184.
(35) Dronskowski, R.; Bloechl, P. E. Crystal Orbital Hamilton Populations (COHP): Energy-Resolved Visualization of Chemical Bonding in Solids Based on Density-Functional Calculations. *J. Phys. Chem.* **1993**, *97*, 8617−8624.
(36) Deringer, V. L.; Tchougréeff, A. L.; Dronskowski, R. Crystal Orbital Hamilton Population (COHP) Analysis As Projected from Plane-Wave Basis Sets. *J. Phys. Chem. A* **2011**, *115*, 5461−5466.
(37) Maintz, S.; Deringer, V. L.; Tchougréeff, A. L.; Dronskowski, R. Analytic Projection from Plane-Wave and PAW Wavefunctions and Application to Chemical-Bonding Analysis in Solids. *J. Comput. Chem.* **2013**, *34*, 2557−2567.
(38) Maintz, S.; Deringer, V. L.; Tchougréeff, A. L.; Dronskowski, R. LOBSTER: A Tool to Extract Chemical Bonding from Plane-Wave Based DFT. *J. Comput. Chem.* **2016**, *37*, 1030−1035.
(39) Nelson, R.; Ertural, C.; George, J.; Deringer, V. L.; Hautier, G.; Dronskowski, R. LOBSTER: Local Orbital Projections, Atomic Charges, and Chemical-Bonding Analysis from Projector-Augmented-Wave-Based Density-Functional Theory. *J. Comput. Chem.* **2020**, *41*, 1931−1940.
(40) Klepp, K. O.; Sturmayr, D. Crystal Structure of Sodium Copper Triselenohafnate(IV), $NaCuHfSe_3$. *Z. Kristallogr.—New Cryst. Struct.* **1997**, *212*, 75.
(41) Kolb, A.; Klepp, K. O. Quaternary Chalcogenides of the IVa Metals with Layered Structures: Preparation and Crystal Structure of $NaCuHf_2Se_5$. *Solid State Sci.* **2003**, *5*, 1027−1031.
(42) Sankar, C. R.; Assoud, A.; Kleinke, H. New Layered-Type Quaternary Chalcogenides, Tl_2PbMQ_4 (M = Zr, Hf; Q = S, Se): Structure, Electronic Structure, and Electrical Transport Properties. *Inorg. Chem.* **2013**, *52*, 13869−13874.
(43) Assoud, A.; Kleinke, H. Unique Barium Selenostannate-Selenide: $Ba_7Sn_3Se_{13}$ (and Its Variants $Ba_7Sn_3Se_{13-\delta}Te_\delta$) with $SnSe_4$ Tetrahedra and Isolated Se Anions. *Chem. Mater.* **2005**, *17*, 4509−4513.
(44) Nian, L.; Huang, J.; Wu, K.; Su, Z.; Yang, Z.; Pan, S. $BaCu_2M^{IV}Q_4$ (M^{IV} = Si, Ge, and Sn; Q = S, Se): Synthesis, Crystal Structures, Optical Performances and Theoretical Calculations. *RSC Adv.* **2017**, *7*, 29378−29385.
(45) Pocha, R.; Johrendt, D. Crystal Structures of $Sr_4Sn_2Se_9$ and $Sr_4Sn_2Se_{10}$ and the Oxidation State of Tin in an Unusual Geometry. *Inorg. Chem.* **2004**, *43*, 6830−6837.
(46) Pauling, L. Atomic Radii and Interatomic Distances in Metals. *J. Am. Chem. Soc.* **1947**, *69*, 542−553.
(47) Tranchitella, L. J.; Fettinger, J. C.; Dorhout, P. K.; Van Calcar, P. M.; Eichhorn, B. W. Commensurate Columnar Composite Compounds: Synthesis and Structure of $Ba_{15}Zr_{14}Se_{42}$ and $Sr_{21}Ti_{19}Se_{57}$. *J. Am. Chem. Soc.* **1998**, *120*, 7639−7640.
(48) Jana, S.; Ishtiyak, M.; Mesbah, A.; Lebègue, S.; Prakash, J.; Malliakas, C. D.; Ibers, J. A. Synthesis and Characterization of $Ba_2Ag_2Se_2(Se_2)$. *Inorg. Chem.* **2019**, *58*, 7837−7844.
(49) Sopiha, K. V.; Comparotto, C.; Marquez, J. A.; Scragg, J. J. S. Chalcogenide Perovskites: Tantalizing Prospects, Challenging Materials. *Adv. Opt. Mater.* **2022**, *10*, 2101704.
(50) Hautier, G.; Ong, S. P.; Jain, A.; Moore, C. J.; Ceder, G. The Accuracy of Density Functional Theory in Predicting Formation Energies of Ternary Oxides from Binary Oxides and its Implication on Phase Stability. *Phys. Rev. B: Condens. Matter Mater. Phys.* **2012**, *85*, 155208.
(51) Bartel, C. J.; Weimer, A. W.; Lany, S.; Musgrave, C. B.; Holder, A. M. The Role of Decomposition Reactions in Assessing First-Principles Predictions of Solid Stability. *npj Comput. Mater.* **2019**, *5*, 4.
(52) Swarnkar, A.; Mir, W. J.; Chakraborty, R.; Jagadeeswararao, M.; Sheikh, T.; Nag, A. Are Chalcogenide Perovskites an Emerging Class of Semiconductors for Optoelectronic Properties and Solar Cell? *Chem. Mater.* **2019**, *31*, 565−575.
(53) Müller, P. C.; Ertural, C.; Hempelmann, J.; Dronskowski, R. Crystal Orbital Bond Index: Covalent Bond Orders in Solids. *J. Phys. Chem. C* **2021**, *125*, 7959−7970.

https://doi.org/10.1021/acs.inorgchem.4c00363
Inorg. Chem. 2024, 63, 6474−6482